Photo-Kelvin probe force microscopy for photocatalytic performance characterization of single filament of TiO₂ nanofiber photocatalysts†

Ming-Chung Wu,*[a] Hseuh-Chung Liao,[b] Yu-Cheng Cho,[c] Géza Tóth,[d] Yang-Fang Chen,[c] Wei-Fang Su[b] and Krisztián Kordás[de]

This is an in-depth study on the photocatalytic performance characterization for single filament of TiO₂ nanofiber photocatalysts by the novel photo-Kelvin probe force microscopy technique (photo-KPFM) and first principles calculations. Three kinds of TiO₂ nanofibers: anatase TiO₂ nanofibers (anatase TiO₂ NFs), nitrogen doped TiO₂ nanofibers (N-TiO₂ NFs), and nitrogen doped TiO₂ nanofibers decorated with platinum nanoparticles (N-TiO₂-Pt NFs) were investigated. The N-TiO₂-Pt NFs exhibit the largest negative photo surface potential shift (−182 mV) as compared to anatase TiO₂ NFs (−29 mV). The first-principles calculations based on density functional theory (CASTEP simulation software) indicate that the significant photo surface potential shift obtained by adding nitrogen and platinum into TiO₂ NFs is induced by two mechanisms: (1) enhancement in absorbance to increase exciton generation and (2) decreased charge recombination to increase surface charge. These changes in the photo surface potential of various TiO₂ nanofibers are closely correlated with their photocatalytic activity. Thus, this novel photo-KPFM provides a useful technique to easily monitor the photocatalytic capability of materials in the development of high performance photocatalysts.

Introduction

TiO₂ and its derivatives are very important materials due to their availability, low cost, chemical stability, *etc.* Their applications in dye-sensitized solar cells,[1,2] polymer hybrid solar cells,[3,4] photocatalytic hydrogen production and photocatalytic degradation of organics[5–8] have been widely studied. Nitrogen doped n-type TiO₂ exhibits decreased band gap due to the mixing of N 2p states with O 2p states, and shows photodegradation capability toward methylene blue and gaseous acetaldehyde by visible light.[9] In addition, a Schottky interface is formed between metal nanoparticles with large work function (such as Pt, Pd, and Au) and n-type TiO₂, while p-type semiconductors in

contact with TiO₂ result in p–n junctions at the interface. Since both types of junctions have a rectifying electrical transport behaviour, an efficient charge separation of the photogenerated electron–hole pairs is achieved, which prevents the undesired electron–hole recombination.[10–12] Hydrothermal synthesis of various types of titanate nanomaterials opened up new possibilities for large scale and simple production of self-similar TiO₂ photocatalytic materials. This process is robust and enables the synthesis of various titania derivatives *via* the combination of different post-processing methods of titanates including ion-exchange, calcination, doping and surface decoration.[13–17] Additionally, among the titanate and titania nanomaterials, nanofiber-based TiO₂ attracts great attention due to the versatility of post-processing, enabling the formation of large area films, coatings, and porous membranes as well as composites with polymers.[17–19]

Recently, Kelvin probe force microscopy (KPFM) has been used to obtain simultaneous mapping of structural and electronic properties of conjugated polymer based photovoltaic materials. The KPFM technique adopts a non-contacting tip with a conductive coating to measure the surface potential difference between the tip and the local surface.[20,21] Previously, Samorì *et al.* reported that KPFM has the ability to obtain quantitative mappings in a non-contacting and non-destructive manner, which is quite suitable for sensitive organic materials.[22] Su *et al.* demonstrated the utilization of KPFM to correlate the surface potential shifts with the power conversion

[a]*Department of Chemical and Materials Engineering, Chang Gung University, Taoyuan 33302, Taiwan. E-mail: mingchungwu@mail.cgu.edu.tw; Tel: +886 3 2118800 ext. 3545*

[b]*Department of Materials Science and Engineering, National Taiwan University, Taipei 10617, Taiwan*

[c]*Department of Physics, National Taiwan University, Taipei 10617, Taiwan*

[d]*Microelectronics and Materials Physics Laboratories, Department of Electrical Engineering, University of Oulu, Oulu FIN-90014, Finland*

[e]*Technical Chemistry, Department of Chemistry, Chemical-Biological Center, Umeå University, SE-901 87 Umeå, Sweden*

† Electronic supplementary information (ESI) available: Schematic illustration of photo-KPFM measurement. Theoretical band gap for TiO₂-based materials. Structure of TiO₂ NFs in a 2 × 3 × 1 supercell. Theoretical absorption spectrum of TiO₂, N-TiO₂ NFs and N-TiO₂-Pt NFs. Density of states of TiO₂, N-TiO₂ and N-TiO₂-Pt NFs. See DOI: 10.1039/c3ta01011b

This journal is © The Royal Society of Chemistry 2013

J. Mater. Chem. A, 2013, **1**, 5715–5720 | **5715**

efficiency of a P3HT–TiO$_2$ nanorod hybrid bulk heterojunction.[23] Spadafora *et al.* adopted a KPFM technique under ultrahigh vacuum to study P3HT/PCBM photovoltaic devices, and the spatial resolution achieved representing ten times improvement over previous study.[24] As demonstrated by the above examples, KPFM is a robust technique which can provide information on the evolution of carrier distribution and on the change of band structure of thin films. While the technique has been widely used in the investigation of electronic properties of photovoltaic materials, the adoption for characterizing inorganics, particularly photocatalytic materials, is still rare. Therefore, in this study, we implement photo-KPFM, which combines illumination with the KPFM technique, to measure the photo surface potential shift of single filament of TiO$_2$-based nanofibers. By analyzing the surface potential shift of individual TiO$_2$-based nanofibers with and without illumination, we found that the photo surface potential shifts of TiO$_2$-based nanofibers are proportional to the photocatalytic activity, which can serve as an index to indicate the photocatalytic activity.

Furthermore, simulation by first-principles calculations is a useful tool to predict electron transfer and exciton dissociation at the atomic level. Previously, Varley *et al.* used such models to study the controversial mechanism of enhanced photocatalytic activity of nitrogen doped TiO$_2$ and demonstrated the importance of impurity level-to-band transitions.[25] Sun *et al.* adopted first-principles calculations to determine the reaction mechanism of water splitting on GaN, and showed that the first hydrogen splitting is catalysed by the GaN surface.[26] Diebold and co-workers reported that the degrees of hydroxylation are important to catechol diffusion over the TiO$_2$ (110) surface. Accordingly, first-principles calculations are proved to be a useful tool to examine the mechanism behind impurities and reduction in surface potential.[27] In the present study, we also perform first-principles calculations to clarify the photocatalytic mechanism of TiO$_2$ nanofibers. The results show considerable consistency with those obtained using the photo-KPFM analysis (and photocatalytic activity measurements reported earlier).

Experimental section

Preparation of TiO$_2$ NFs

TiO$_2$ NFs used in this work were the same as those reported earlier.[28] First, sodium titanate (Na$_2$Ti$_y$O$_{2y+1}$) nanofibers were synthesized by the hydrothermal method from anatase in 10 M NaOH (aq.) at 175 °C for 24 h in a rotating autoclave with 120 rpm revolving around its short axis. The product was washed in 0.1 M HCl to replace Na$^+$ ions with protons and was then rinsed in deionized water followed by filtering and drying in air at 70 °C. The as-obtained product is H$_{2-x}$Na$_x$Ti$_y$O$_{2y+1}$ (Na concentration of 8.54 at% by XPS). TiO$_2$ NFs were obtained by calcination of the sodium hydrogen nanofibers at 600 °C for 12 h to form TiO$_2$ anatase nanofibers. N-TiO$_2$ NFs were also synthesized from Na$_2$Ti$_y$O$_{2y+1}$ nanofibers but in two subsequent calcination steps: first, calcination in air at 600 °C for 12 h to form TiO$_2$ anatase nanofibers, followed by a second calcination step in ammonia gas (50 mL min^{-1}, 2% NH$_3$ in N$_2$ buffer) at the same temperature

for 3 h. The as-prepared N-TiO$_2$ NFs were subsequently decorated with Pt nanoparticles. In a typical process, 20.4 mg of platinum(II) acetylacetonate (Aldrich, 99.99%) was dissolved in 100 mL of acetone and mixed with 1.0 g of N-TiO$_2$ NFs by ultrasonic agitation for 3 h and stirring for 6 h. After evaporating the solvent (at ~80 °C hotplate temperature) under a N$_2$ flow, the samples were calcined in air at 300 °C for 2 h, and then reduced in a 15% H$_2$ (in Ar buffer) flow at 500 °C for 4 h to obtain N-TiO$_2$-Pt NFs with ~1.0 wt% Pt metal load.

Characterization of TiO$_2$ NFs

The microstructures of diameter/structure of anatase TiO$_2$ NFs, N-TiO$_2$ NFs, and N-TiO$_2$-Pt NFs were studied by high-resolution transmission electron microscopy (JEOL 2000FX, 200 kV, LaB6 gun) as well as by synchrotron X-ray spectroscopy ($\lambda \sim 1.025$ Å) on beam line 13A1 of the National Synchrotron Radiation Research Center (NSRRC) in Taiwan.

Photo-KPFM analysis

The surface potential mapping was measured using a photo-KPFM (Kelvin probe force microscope, Digital Instruments, Nanoscopes III). The TiO$_2$ nanofibers were dispersed in ethanol and then spin-coated on an Au substrate. The experimental setup of photo-KPFM (ESI, Fig. S1†) was constructed by placing a UV-B light ($\lambda_{max} \sim 312$ nm, 8 watts) next to the KPFM (Digital Instrument, Nanoscopes III). The surface potential maps of samples were taken by this photo-KPFM with and without illumination at room temperature. N-type silicon cantilever (Nanosensors) with high softness (average force constant of ~2.8 N m^{-1}) and with a resonance frequency of 75 kHz on average is coated with chromium, as a buffering layer, and a platinum–iridium5 alloy, as a conductive layer, was used. Anatase TiO$_2$ NFs, N-TiO$_2$ NFs, and N-TiO$_2$-Pt NFs were dispersed in ethanol and spin-coated on a 100 nm thick gold-coated silicon wafer. After drying, the samples were measured by photo-KPFM. With this method, the height variation and contact potential by electrostatic force between the conductive tip and the surface of the samples are measured simultaneously. A line is scanned using AFM in tapping mode to acquire the topographic information of the material, then the same line is rescanned with the tip lifted to a height of 20 nm. During the second scan, V_{DC} is applied at the tip to nullify the electrostatic oscillations, position by position, and the contact potential difference is observed and measured. The surface potential distribution of the TiO$_2$-based NFs was mapped in the dark or under the illumination of a UV-B lamp (Sankyo Denki, G8T5E, 8 W). In addition, the function of the cross-section analysis was used to get detailed information on the topographic height and the surface potential across the selected line. After analyzing these data, the surface potential in the dark or under UV-B illumination was obtained. The surface potential difference is then denoted as the photo surface potential shift.

Computational simulation

Computational simulation used in this paper is based on density functional theory with a GGA-PBE (Generalized

5716 | *J. Mater. Chem. A*, 2013, **1**, 5715–5720

This journal is © The Royal Society of Chemistry 2013

Gradient Approximation Perdew–Burke–Ernzerhof) functional implemented in CASTEP (Cambridge Serial Total Energy Package) which uses a plane wave basis set to expand the election wave function. As for the pseudopotential, two different setups are adopted depending on the characteristic we are simulating. This is because that different pseudopotential will have better accuracy in predicting the properties they suit. In the simulations of band gap, density of states (DOS) and absorption spectrum, TiO_2 is modeled by a ($2 \times 3 \times 1$) supercell doped with different impurities (N and Pt) (ESI, Fig. S2†). In this case, a norm-conserving pseudopotential is used due to its accuracy in predicting optical properties, and the calculations are conducted with an energy cutoff of 450.0 eV and a k-point set of $1 \times 1 \times 2$. In the simulations of electron density difference, a supercell of ($3 \times 1 \times 1$) TiO_2 crystal is used to simulate the electronic behavior. An ultrasoft pseudopotential is chosen in this simulation and calculations are conducted with an energy cutoff of 300.0 eV and a k-point set of $1 \times 1 \times 2$.

Results and discussion

High resolution TEM images and synchrotron X-ray spectra of various TiO_2-based NFs show a highly crystalline anatase phase as shown in Fig. 1. The as-prepared anatase TiO_2 NFs have lengths of up to a few micrometers and diameters of ~50 to 100 nm (the inset of Fig. 1(a)). N-TiO_2 NFs prepared by the two-step calcination are shown in Fig. 1(b). The (101) spacing of both anatase TiO_2 NFs and N-TiO_2 NFs is about 3.40 Å, indicating that the two-step calcination method did not cause considerable expansion of the lattice. Based on TEM analysis, the Pt nanoparticles are homogeneously distributed on the surface of N-TiO_2-Pt NFs with an average particle diameter of 1.9 ± 0.3 nm as shown in Fig. 1(c). The synchrotron X-ray spectra ($\lambda \sim 1.025$ Å) show that TiO_2-based nanofibers are still in the anatase phase with negligible effect of N-doping on the structure (Fig. 1(d)). The weak and broadened XRD reflections found at $2\theta \sim 26.4°$ for N-TiO_2-Pt NFs can be assigned to

metallic Pt(111), and suggest that very small size Pt nanoparticles are present (Fig. 1(e)).

Topographic images and surface potential mappings of single filament of anatase TiO_2 NFs, N-TiO_2 NFs and N-TiO_2-Pt NFs with/without illumination were investigated by KPFM as shown in Fig. 2. These TiO_2-based NFs were dispersed in ethanol and then deposited on a 100 nm thick gold coated silicon wafer by spin coating in order to obtain well-separated individual filaments of the nanofibers. Fig. 2(a), (d) and (g) show the topographic images, Fig. 2(b), (e) and (h) are the surface potential maps without illumination, Fig. 2(c), (f) and (i) are the surface potential maps under UV-B irradiation of individual filaments of anatase TiO_2, N-TiO_2 and N-TiO_2-Pt, respectively. The Fermi energy (E_f) of the Au substrate (~5.2 eV relative to
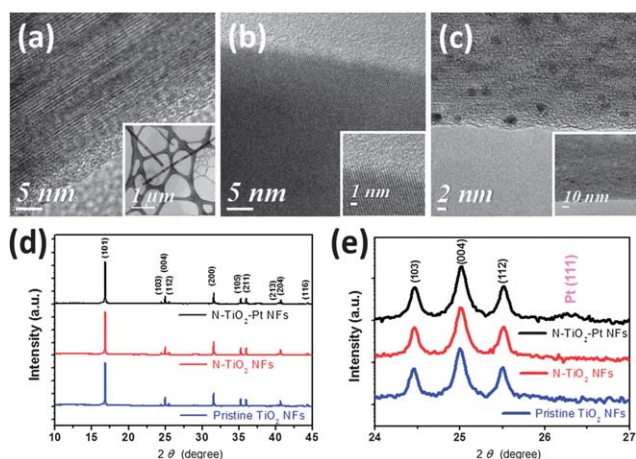

Fig. 1 High resolution TEM images of (a) anatase TiO_2 NFs, (b) N-TiO_2 NFs and (c) N-TiO_2-Pt NFs. Synchrotron X-ray spectra of TiO_2-based NFs with different scanning rates: (d) fast scanning rate of 0.04 degree per second and (e) slow scanning rate of 0.004 degree per second.
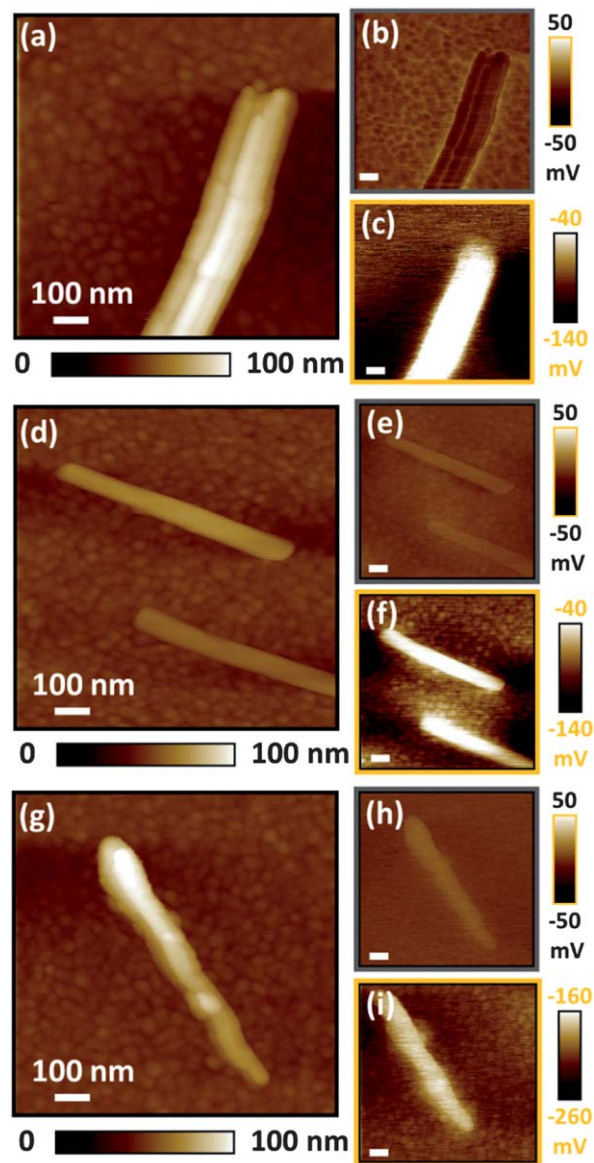

Fig. 2 Surface topographic images (a, d and g) and surface potential mappings in the dark (b, e and h) or under UV-B illumination (c, f and i) of three kinds of TiO_2-based nanofibers: anatase TiO_2 NFs (a–c), N-TiO_2 NFs (d–f) and N-TiO_2-Pt NFs (g–i). The white scale bar indicates 100 nm.

vacuum) served as a reference in order to examine E_f of the different types of nanowires. Ideally, E_f of TiO_2-based nanofibers and Au substrates without illumination should match thus leading to uniform surface potentials across the mapping images. Consequently, equal surface potential between Au/N-TiO_2 NFs and Au/N-TiO_2-Pt NFs can be observed in Fig. 2(e) and (h) respectively. However, it can be observed that the surface potential of anatase TiO_2 NFs (Fig. 2(b)) without illumination is slightly lower than that of the Au substrate by approximately 15 mV, indicating the partially residual negative charges remaining on the surface of anatase TiO_2 NFs.

TiO_2 is considered as an n-type semiconductor and electron–hole pairs can be generated under ultraviolet light irradiation. In the present work, UV-B light with a λ_{max} of 312 nm was used to irradiate the TiO_2-based nanofibers. It results in the splitting of E_f into quasi-Fermi energy, E_{fn} and E_{fp}, for electrons and holes respectively. E_{fn} is usually considered in TiO_2 because of its characteristic as an n-type semiconductor with electrons being the majority carriers. When TiO_2-based nanofibers are illuminated by UV-B, the generated electron–hole pairs can be dissociated in the presence of a redox couple leaving holes on the TiO_2 surfaces for further oxidation and generation of OH radicals. The processes of carrier generation, carrier dissociation and carrier transfer directly determine the photocatalytic performance. Moreover, the presence of the redox couple Au substrates facilitates the electron–hole pair dissociation, i.e. the electrons can transfer from TiO_2-based nanofibers to Au substrates. Fig. 2(c), (f) and (i) show the surface potential mapping for anatase TiO_2 NFs, N-TiO_2 NFs and N-TiO_2-Pt NFs with UV-B illumination respectively. Generally, for all TiO_2-based nanofibers, the average surface potential with illumination shows a negative shift compared to those without illumination. It suggests that the electron–hole pairs can be generated under UV-B light leading to an upward shift of Fermi energy from E_f to E_{fn} and thus the detected negative shift of surface potential. Above all, the most significant shift in N-TiO_2-Pt NF ($\sim$−180 mV) mapping was obtained indicating the largest population of accumulated photo-generated carriers. Additionally, the non-equilibrated Fermi energy between TiO_2-based nanofibers and Au substrates further implies the occurrence of a carrier transfer process (electron–hole pair dissociation) between the redox couple under UV-B illumination. From Fig. 2, we find that anatase TiO_2 NFs and N-TiO_2 NFs have a larger photo surface potential shift than N-TiO_2-Pt NFs due to the presence of Pt nanoparticles decorating the TiO_2 nanofibers. Namely, the Pt nanoparticles provide an alternative center for electron–hole pair dissociation, competing with the Au substrate. As a consequence, besides electron injection to the gold (Au) substrate, the separated electrons can also be trapped by Pt nanoparticles and remain close to the TiO_2 surface, leading to a lowered surface potential difference between redox couple.

In order to visualize the photo surface potential variation even better, the UV-B light was switched on then off during scanning. The obtained photo surface potential mappings (Fig. 3(a), (c) and (e)) clearly show the significant negative surface potential shifts of the Au substrate upon illumination
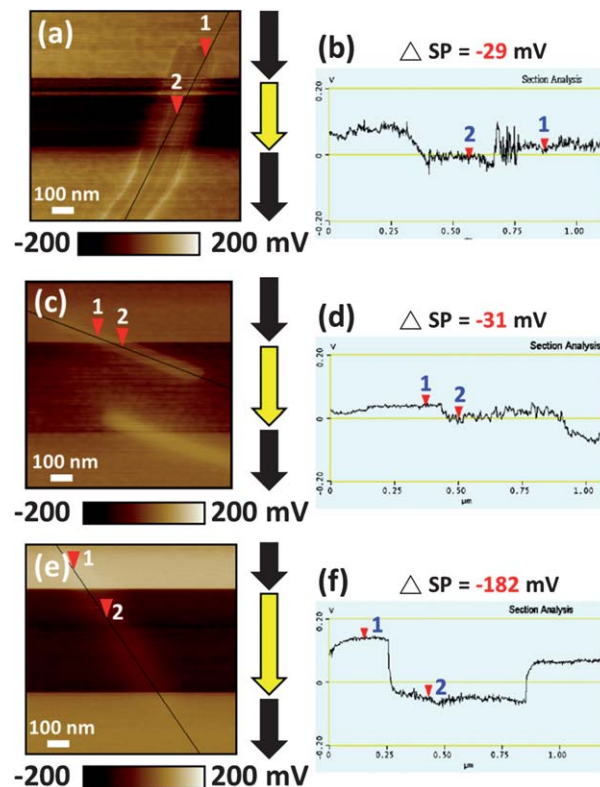

Fig. 3 Photo surface potential mappings (a, c and e) and the cross-section profiles (b, d and f) of nanofiber's surface potential of three kinds of TiO_2-based nanofibers: (a and b) anatase TiO_2 NFs, (c and d) N-TiO_2 NFs and (e and f) N-TiO_2-Pt NFs.

due to the accumulation of electrons injected from the nanofibers. Considering the surface potential variation of nanofibers as shown in the surface potential profile across the nanofibers (Fig. 3(b), (d) and (f)), all the three kinds of TiO_2 nanofibers reveal a dropped surface potential upon illumination based on the same reason of Fermi energy splitting. A considerable drop of surface potential ($\sim$−182 mV) was observed in the case of N-TiO_2-Pt nanofibers, presenting the larger shift of E_{fn} relative to E_f than that of anatase TiO_2 NFs (photo surface potential shift $\sim$ −29 mV) and N-TiO_2 NFs (photo surface potential shift $\sim$ −31 mV). The accumulated electrons in Pt nanoparticles hence caused the decreased surface potential and shifted E_{fn} closer to the TiO_2 conduction band. Correlating with the photocatalytic property, it is known that the transfer of electrons to noble metal nanoparticles can greatly reduce the opportunity of electron–hole recombination and hence significantly improve the photocatalytic property. Therefore, the surface potential shift depicted here can serve as an index to evaluate the photocatalytic property. The rapid redistribution of charge carriers react quickly to switching on and off the UV light, as shown by the sharp steps of surface potential between light and dark conditions (Fig. 3(f)). In conclusion, the correlation between photocatalytic property and the dynamic process of carrier generation, carrier transfer, and carrier accumulation performed by photo-KPFM measurement is demonstrated here for the first time. The photo surface potential mapping of nanomaterials with high resolution can further provide useful

5718 | J. Mater. Chem. A, 2013, **1**, 5715–5720

This journal is © The Royal Society of Chemistry 2013

information of the photocatalysis process for evaluating the photocatalytic activity.

Computer simulation is used to examine the mechanism of photo surface potential shift caused by nitrogen doping with/without platinum decoration. All simulations are based on CASTEP module in Materials Studio developed by Accelrys Software Inc. The theoretical calculations of the band gap and the absorption spectrum of TiO_2-based materials are presented in the ESI, Table S1 and Fig. S3.† The calculated theoretical band gap of anatase TiO_2 is 2.441 eV which is smaller than the experimental value of 3.20 eV.[29] The difference of band gap values originates from the Generalized Gradient Approximation (GGA) Perdew–Burke–Ernzerhof (PBE) functional which is well known to underestimate the band gap of semiconductors.[30] Despite the underestimated value, the calculations are sufficient to compare the variation of band gap in $N-TiO_2$ and $N-TiO_2$-Pt. For $N-TiO_2$, nitrogen doping in interstitial sites was considered (ESI, Fig. S2†) and the band gap of 1.514 eV is obtained, which is significantly smaller than that of anatase TiO_2 (2.441 eV). The doping of nitrogen impurities gives rise to the generation of impurity bands located above the maximum of valence band and hence narrows the band gap (ESI, Fig. S4†). Therefore, enhancement in absorbance can be clearly observed in $N-TiO_2$. However, in $N-TiO_2$-Pt we can observe that an even stronger absorbance occurs with a bandgap similar to $N-TiO_2$. This may be due to the strong Pt resonant surface plasmon coupling and Pt nanoparticle scattering effect to improve the light absorption other than the formation of impurity band alone.[31] From the experimental results and simulation, nitrogen doping and platinum decoration are beneficial to increase the absorbance of TiO_2 materials in the visible region. However, in the case of $N-TiO_2$-Pt, the increased absorbance alone is not sufficient to contribute to the huge photo surface potential shift in Table 1 (approximately half an order increase compared with $N-TiO_2$).

In Fig. 4, electron density differences of TiO_2-based materials are considered which reveal the way how electrons re-distribute before and after the impurities are added to anatase TiO_2. The difference in electron densities is shown in Fig. 4 by dots; and the loss/enrichment of electron density is indicated in blue/red, respectively. When doping with nitrogen, the nitrogen attracts the electrons nearby causing a locally electron rich environment. In contrast, platinum decorated $N-TiO_2$ NFs strongly exclude electrons from their surrounding and increase further the local charge density in the interstitial site. These local positive or negative charges are considered to attract and separate the electrons and holes after electron–hole-pairs generation. Therefore, the added dopant increases the attractive sites and reduces the probability of electron–hole recombination.
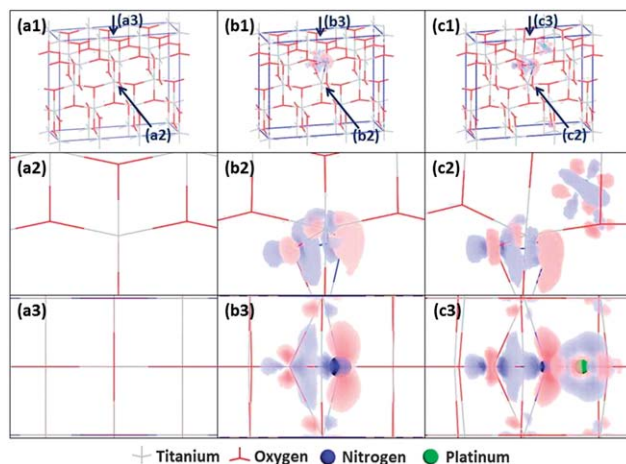

Fig. 4 Structures and images of electron density difference for (a) TiO_2, (b) $N-TiO_2$ and (c) $N-TiO_2$-Pt. (a1, b1 and c1) General view of the structure with Ti and oxygen indicated as gray and red balls, (a2, b2 and c2) top view of the respective structure, and (a3, b3 and c3) side view of the respective structure. In (b) and (c) nitrogen dopant is arbitrarily built in the interstitial site of oxygen due to the periodic properties of CASTEP. The "electron density difference" is the difference of total electron densities between "after" and "before" the dopant is introduced to this TiO_2 set and it indicates how the electrons will be distributed after TiO_2 is doped.

Consequently, more electrons diffuse to the surface of TiO_2, leading to a larger surface potential shift as also shown by KPFM. On the other hand, when platinum is on the surface of the semiconductor, the decreased opportunity of the electron–hole pair recombination should be the main reason for the large negative photo surface potential shift (instead of the band gap reduction).

Conclusions

In summary, we have shown that UV-light photo Kelvin probe force microscopy is a useful technique to study light-induced surface charge variation in TiO_2-based materials. Anatase TiO_2 NFs doped with nitrogen and then decorated with Pt nanoparticles have the largest negative surface potential shift (−182 mV) compared to other TiO_2-based NFs, in agreement with the greatest photocatalytic activity for hydrogen production we reported earlier.[28] Simulation data suggest that the significant surface potential shift is due to the red shift of the absorption spectrum and because of the decreased possibility for electron–hole pair recombination.

Acknowledgements

Table 1 Average surface potential of three kinds of TiO_2-based nanofibers

Sample	Photo surface potential shift (mV)	H_2 production rate (μmol g^{-1} h^{-1})[28]
Anatase TiO_2 NFs	−29	150
$N-TiO_2$ NFs	−31	300
$N-TiO_2$-Pt NFs	−182	22 500

Notes and references

1 U. Bach, D. Lupo, P. Comte, J. E. Moser, F. Weissörtel, J. Salbeck, H. Spreitzer and M. Grätzel, *Nature*, 1998, **395**, 583.

2 K.-M. Lee, V. Suryanarayanan and K.-C. Ho, *Sol. Energy Mater. Sol. Cells*, 2007, **91**, 1416.

3 M.-C. Wu, C.-H. Chang, H.-H. Lo, Y.-S. Lin, W.-C. Yen, W.-F. Su, Y.-F. Chen and C.-W. Chen, *J. Mater. Chem.*, 2008, **18**, 4097.

4 T.-W. Zeng, Y.-Y. Lin, H.-H. Lo, C.-W. Chen, C.-H. Chen, S.-C. Liou, H.-Y. Huang and W.-F. Su, *Nanotechnology*, 2006, **17**, 5387.

5 A. Fujishima and K. Honda, *Nature*, 1972, **238**, 37.

6 D. V. Bavykin, J. M. Friedrich and F. C. Walsh, *Adv. Mater.*, 2006, **18**, 2807.

7 X. Qiu, Y. Zhao and C. Burda, *Adv. Mater.*, 2007, **19**, 3995.

8 H. G. Yang, G. Liu, S. Z. Qiao, C. H. Sun, Y. G. Jin, S. C. Smith, J. Zou, H. M. Cheng and G. Q. Lu, *J. Am. Chem. Soc.*, 2009, **131**, 4078.

9 R. Asahi, T. Morikawa, T. Ohwaki, K. Aoki and Y. Taga, *Science*, 2001, **293**, 269.

10 K. Uosaki, R. Yoneda and H. Kita, *J. Phys. Chem.*, 1985, **89**, 4042.

11 X. Chen and S. S. Mao, *Chem. Rev.*, 2007, **107**, 2891.

12 A. Kudo and Y. Miseki, *Chem. Soc. Rev.*, 2009, **38**, 253.

13 D. V. Bavykin, V. N. Parmon, A. A. Lapkin and F. C. Walsh, *J. Mater. Chem.*, 2004, **14**, 3370.

14 E. Horváth, Á. Kukovecz, Z. Kónya and I. Kiricsi, *Chem. Mater.*, 2007, **19**, 927.

15 P. Zhang, S. Yin, V. Petrykin, M. Kakihana and T. Sato, *J. Mol. Catal. A: Chem.*, 2009, **309**, 50.

16 T. P. Feist and P. K. Davies, *J. Solid State Chem.*, 1992, **101**, 275.

17 M.-C. Wu, A. Sápi, A. Avila, M. Szabó, J. Hiltunen, M. Huuhtanen, G. Tóth, Á. Kukovecz, Z. Kónya, R. Keiski, W.-F. Su, H. Jantunen and K. Kordás, *Nano Res.*, 2011, **4**, 360.

18 W. Dong, A. Cogbill, T. Zhang, S. Ghosh and Z. R. Tian, *J. Phys. Chem. B*, 2006, **110**, 16819.

19 K. Woan, G. Pyrgiotakis and W. Sigmund, *Adv. Mater.*, 2009, **21**, 2233.

20 V. Palermo, M. Palma and P. Samorì, *Adv. Mater.*, 2006, **18**, 145.

21 H. Hoppe, T. Glatzel, M. Niggemann, A. Hinsch, M. C. Lux-Steiner and N. S. Sariciftci, *Nano Lett.*, 2005, **5**, 269.

22 A. Liscio, G. D. Luca, F. Nolde, V. Palermo, K. Müllen and P. Samorì, *J. Am. Chem. Soc.*, 2008, **130**, 780.

23 M.-C. Wu, Y.-J. Wu, W.-C. Yen, H.-H. Lo, C.-F. Lin and W.-F. Su, *Nanoscale*, 2010, **2**, 1448.

24 E. J. Spadafora, R. Demadrille, B. Ratier and B. Grévin, *Nano Lett.*, 2010, **10**, 3337.

25 J. B. Varley, A. Janotti and C. G. Van de Walle, *Adv. Mater.*, 2011, **23**, 2343.

26 P.-T. Chen, C.-L. Sun and M. Hayashi, *J. Phys. Chem. C*, 2010, **114**, 18228.

27 S.-C. Li, L.-N. Chu, X.-Q. Gong and U. Diebold, *Science*, 2010, **328**, 882.

28 M.-C. Wu, J. Hiltunen, A. Sápi, A. Avila, W. Larsson, H.-C. Liao, M. Huuhtanen, G. Tóth, A. Shchukarev, N. Laufer, Á. Kukovecz, Z. Kónya, J.-P. Mikkola, R. Keiski, W.-F. Su, Y.-F. Chen, H. Jantunen, P. M. Ajayan, R. Vajtai and K. Kordás, *ACS Nano*, 2011, **5**, 5025.

29 D. Zhao, X. Huang, B. Tian, S. Zhou, Y. Li and Z. Dua, *Appl. Phys. Lett.*, 2011, **98**, 162107.

30 M. V. Ganduglia-Pirovano, A. Hofmann and J. Sauer, *Surf. Sci. Rep.*, 2007, **62**, 219.

31 J. M. Lin, H. Y. Lin, C. L. Cheng and Y. F. Chen, *Nanotechnology*, 2006, **17**, 4391.